

# A MULTI-CHORD STELLAR OCCULTATION BY THE LARGE TRANS-NEPTUNIAN OBJECT (174567) VARDA

D. Souami<sup>1,2</sup>, F. Braga-Ribas<sup>3,1,4,5</sup>, B. Sicardy<sup>1</sup>, B. Morgado<sup>1,5</sup>, J. L. Ortiz<sup>6</sup>, J. Desmars<sup>7,8</sup>, J.I.B. Camargo<sup>4,5</sup>,  
F. Vachier<sup>8</sup>, J. Berthier<sup>8</sup>, B. Carry<sup>9</sup>, C.J. Anderson<sup>10,11</sup>, R. Showers<sup>11</sup>, K. Thomason<sup>11</sup>, P. D. Maley<sup>10,12</sup>,  
W. Thomas<sup>10</sup>, M. W. Buie<sup>13</sup>, R. Leiva<sup>13</sup>, J.M. Keller<sup>14</sup>, R. Vieira-Martins<sup>4,5,8</sup>, M. Assafin<sup>15,5</sup>, P. Santos-Sanz<sup>6</sup>,  
N. Morales<sup>6</sup>, R. Duffard<sup>6</sup>, G. Benedetti-Rossi<sup>1,5</sup>, A.R. Gomes-Júnior<sup>16,5</sup>, R. Bouffleur<sup>4,5</sup>, C.L. Pereira<sup>3,5</sup>, G. Margoti<sup>3</sup>,  
H. Pavlov<sup>10,17</sup>, T. George<sup>10</sup>, D. Oesper<sup>10</sup>, J. Bardecker<sup>10</sup>, R. Dunford<sup>10,21</sup>, M. Kehrli<sup>18</sup>, C. Spencer<sup>18</sup>, J.M. Cota<sup>19</sup>,  
M. Garcia<sup>19</sup>, C. Lara<sup>19</sup>, K.A. McCandless<sup>19</sup>, E. Self<sup>19</sup>, J. Lecacheux<sup>1</sup>, E. Frappa<sup>20</sup>, D. Dunham<sup>10</sup>, M. Emilio<sup>22</sup>.

<sup>1</sup> LESIA UMR-8109, Observatoire de Paris, Université PSL, CNRS, Sorbonne Université, Univ. Paris Diderot, Sorbonne Paris Cité, 5 place Jules Janssen, 92195 Meudon, France

<sup>2</sup> naXys, University of Namur, Rempart de la Vierge, Namur, B-5000, Belgium

<sup>3</sup> Federal University of Technology - Paraná (UTFPR / DAFIS), Curitiba, Brazil

<sup>4</sup> Observatório Nacional/MCTIC, Rio de Janeiro, Brazil

<sup>5</sup> Laboratório Interinstitucional de e-Astronomia - LineA, Rua Gal. José Cristino 77, Rio de Janeiro, RJ, 20921-400, Brazil

<sup>6</sup> Instituto de Astrofísica de Andalucía, IAA-CSIC, Glorieta de la Astronomía s/n, 18008 Granada, Spain

<sup>7</sup> Institut Polytechnique des Sciences Avancées IPSA, 63 boulevard de Brandebourg, F-94200 Ivry-sur-Seine, France

<sup>8</sup> IMCCE-CNRS UMR8028, Observatoire de Paris, PSL Université, Sorbonne Université, 77 Av. Denfert-Rochereau, 75014 Paris, France

<sup>9</sup> Université de la Côte d'Azur, Observatoire de la Côte d'Azur, CNRS, Laboratoire Lagrange, France

<sup>10</sup> International Occultation Timing Association (IOTA)

<sup>11</sup> College of Southern Idaho, USA

<sup>12</sup> NASA Johnson Space Center Astronomical Society, USA

<sup>13</sup> Southwest Research Institute, 1050 Walnut St., Suite 300, Boulder, CO 80302, USA

<sup>14</sup> University of Colorado, Boulder, Colorado, USA

<sup>15</sup> Observatório do Valongo/UFRJ, Rio de Janeiro, Brazil

<sup>16</sup> UNESP - São Paulo State University, Grupo de Dinâmica Orbital e Planetologia, Guaratinguetá, SP, 12516-410, Brazil

<sup>17</sup> Tangra Observatory (E24), Australia

<sup>18</sup> California Polytechnic State University, San Luis Obispo, California, USA

<sup>19</sup> Calipatria High School, Calipatria, California, USA

<sup>20</sup> Euraster, 1 rue du tonnelier, 46100 Faycelles, France

<sup>21</sup> Jimginny Observatory (W08), Naperville, IL, USA.

<sup>22</sup> Universidade Estadual de Ponta Grossa (UEPG), Brazil

e-mail: damya.souami@obspm.fr ; souami@astro.utoronto.ca

Received May 31<sup>st</sup>, 2020; accepted July 22<sup>nd</sup>, 2020

## ABSTRACT

**Context.** We present results from the first recorded stellar occultation by the large trans-Neptunian object (174567) Varda that was observed on September 10<sup>th</sup>, 2018. Varda belongs to the high-inclination dynamically excited population, and has a satellite, Ilmarë, which is half the size of Varda.

**Aims.** We determine the size and albedo of Varda and constrain its 3D shape and density.

**Methods.** Thirteen different sites in the USA monitored the event, five of which detected an occultation by the main body. A best-fitting ellipse to the occultation chords provides the instantaneous limb of the body, from which the geometric albedo is computed. The size and shape of Varda are evaluated, and its bulk density is constrained, using Varda's mass known from previous works.

**Results.** The best-fitting elliptical limb has semi-major (equatorial) axis of  $(381 \pm 3)$  km and an apparent oblateness  $0.043 \pm 0.036$  corresponding to an apparent area-equivalent radius  $R'_{\text{equiv}} = (373 \pm 8)$  km and geometric albedo  $p_v = 0.097 \pm 0.004$  assuming a visual absolute magnitude  $H_v = 3.81 \pm 0.01$ . Using three possible rotational periods for the body (4.76 h, 5.91 h, and 7.87 h), we derive corresponding MacLaurin solutions. Furthermore, given the low-amplitude ( $0.06 \pm 0.01$ ) mag of the single-peaked rotational light-curve for the aforementioned periods, we consider the double periods. For the 5.91 h period (the most probable) and its double (11.82 h), we find bulk densities and true oblateness of  $\rho = (1.52 \pm 0.05) \text{ g cm}^{-3}$ ,  $\epsilon = 0.232 \pm 0.036$  and  $\rho = (1.25 \pm 0.04) \text{ g cm}^{-3}$ ,  $\epsilon = 0.079 \pm 0.044$ . However, it must be noted that the other solutions cannot be excluded just yet.

**Key words.** Methods: observational - Occultations - Kuiper belt objects, individual: Varda.

## 1. Introduction

Stellar occultations are one of the most accurate ground-based methods to directly determine the size and shape of solar system objects, down to kilometric accuracies. In addition, these rare events can be used, amongst others, to reveal the existence of atmospheres, cometary activity, satellites or ring systems around minor planets (Ortiz et al. 2020). We can cite here the discovery of rings around the Centaur (10199) Chariklo (Braga-Ribas et al. 2014) and the dwarf-planet (136108) Haumea (Ortiz et al. 2017) as well as the detection of (87) Sylvia’s satellites (Vachier et al. 2019).

In this paper, we report results obtained from a quintuple-chord occultation event involving Trans-Neptunian Object (174567) Varda (formally 2003 MW<sub>12</sub>). The event was observed on September 10<sup>th</sup>, 2018, and is the first-ever observed stellar occultation by this body; it is used to constrain Varda’s size, 3D shape, geometric albedo, and bulk density. This campaign was carried out within the LUCKY STAR programme<sup>1</sup>, which aims at studying and characterising objects of the outer Solar System object, in particular Centaurs and Trans-Neptunian Objects (TNOs) in collaboration with the RECON project (Buie & Keller 2016).

Varda belongs to the hot classical TNO population. Moreover, it is a binary object, its satellite Ilmarë having about half of its size (Grundy et al. (2015)). As such, the mass of the system can be derived from Kepler’s law thus giving a direct access to Varda’s bulk density, once the volume is pinned down using stellar occultations. Density measurements, in turn, contain clues of the conditions in the primordial solar system and/or the current internal structure of the body and other TNOs similar to Varda (Fernández 2020a; Barucci & Merlin 2020).

A review on Trans-Neptunian Binaries (TNB) is given by Noll et al. (2020). These authors outline the current understanding and progress in the study of TNBs from the identification of binaries, determination of their mutual orbits, measurements of the system’s mass, density, rotational state, component colours, mutual events as well as the shapes. They report on 86 known TNBs at the time of writing. There are now 107 known binary and multiple systems in the TNO population (including Pluto and Charon) with one or more companions<sup>2</sup>.

This paper is organised as follows. Section 2 provides an overview of the Varda-Ilmarë system. Section 3 describes our occultation prediction approach. Section 4 presents the data, and the derived timings for each of the positive chords. In Section 5, Varda’s projected size and geometric albedo are obtained and its 3D shape and density are constrained, and implications are discussed. Section 6 concludes the paper.

## 2. The Varda system, an overview

### 2.1. Varda’s physical properties

Varda was discovered on June 21<sup>st</sup>, 2003 with the 0.9-m Spacewatch telescope at Kitt Peak Observatory (Larsen et al. 2007). A satellite was discovered around it in 2009, see sub-Section 2.2. Varda’s system physical properties, available in the literature, are summarised in Table 1. With an inclination of  $i = 21.5^\circ$  with respect to the Ecliptic plane, Varda falls into the category of the dynamically hot population, characterised by inclinations larger than  $5^\circ$  (Fernández 2020b).

Following the new TNO taxonomy, which is based on colour indices (B-V, V-R, V-I, V-J, V-H, and V-K see Barucci et al. 2005; Fulchignoni et al. 2008), four classes are distinguished with increasingly red colours BB (neutral colour), BR, IR, and RR (very red). Using visible colour photometry, and applying this new taxonomy, Perna et al. (2010) have re-classified Varda as an IR object. After conducting a study on 75 known Centaurs and TNOs, Barucci et al. (2011) found that IR class objects belong to classical and resonant populations. None of the objects they have identified in this class, including Varda, seemed to contain an unambiguous water ice signatures near  $1.5 \mu\text{m}$  and  $2 \mu\text{m}$ . Furthermore, Varda showed the largest positive slope in the  $2.05\text{-}2.3 \mu\text{m}$  range. The spectrum obtained by Barucci et al. (2011) is consistent with the presence of ice tholin on Varda’s surface.

### 2.2. Varda’s satellite, Ilmarë

The Hubble Space Telescope (HST) Snapshot programme 11113 (conducted between July 2007 and April 2009) allowed the observation of 142 TNOs with the Wide Field and Planetary Camera 2 (WFPC2). HST images obtained on April 26, 2009 revealed Varda’s satellite, Ilmarë, at a separation of about 0.12 arcsec (corresponding to  $\sim 4000$  km, i.e. about 12 Varda radii), with a size of about half that of Varda (Table 1). Additional (visible and near IR) data, acquired between April 2009 and July 2013 with HST, Keck II Telescope, and Gemini North Telescope provided the relative offsets of Ilmarë with respect to Varda at twelve different epochs (Grundy et al. 2015 and references therein).

The derived Ilmarë’s orbit has a mirror-ambiguity, two solutions being possible (cf. Table 1). The ambiguity should be removed by the end of 2020, when new relative positions will allow determining the correct solution, due to the changing aspect of the orbit as seen from Earth.

Furthermore, Grundy et al. (2015) used their HST observations to perform separate photometry of the Varda-Ilmarë system (translated in B, V, I Johnson magnitudes). The B-V magnitudes show that the components are consistent with one another, whereas the V-I magnitudes show an Ilmarë slightly redder than Varda (by  $0.133 \pm 0.062$ ), see Grundy et al. 2015, and references therein). Moreover, Grundy et al. (2015) measured the difference in magnitude between the two components,  $\Delta m = (1.734 \pm 0.042)$  mag.

<sup>1</sup> <https://lesia.obspm.fr/lucky-star/>

<sup>2</sup> See the list of Johnston (2018), <http://www.johnstonsarchive.net/astro/astmoons/am-174567.html>, as of February 25<sup>th</sup>, 2020.

Table 1: Varda’s observational, physical, and orbital parameters.

Quantity	Value	Ref.	Comments
Radius (km)	$353^{+41}_{-38}$	V14	Varda’s radius
	$396^{+46}_{-42}$	V14	Effective radius <sup>a</sup> , from radiometric modelling (Herschel data)
	$361^{+41}_{-38}$	G15	Assuming that Varda and Ilmarë have spherical shapes and the same albedo, with brightness difference of $\Delta_{\text{mag}} = 1.734 \pm 0.042$ , using photometric data of HST, Keck II and Gemini North Telescopes, resulting in $R_{\text{Varda}} = 361^{+41}_{-38}$ km and $R_{\text{Ilmarë}} = 163^{+19}_{-17}$ km.
Mass ( $10^{20}$ kg)	$2.664 \pm 0.064$	G15	System’s mass
Geometric albedo	$0.102^{+0.024}_{-0.020}$	V14	Radiometric modelling, Herschel data (“TNOs are Cool programme”)
Absolute magnitude ( $H_V$ )	$3.61 \pm 0.05$	V14	
	$3.988 \pm 0.048$	A16	with a phase coefficient <sup>(b)</sup> $\beta = -0.455 \pm 0.071$
Rotational period (h)	5.9 / 7.87	T10	Single-peaked light-curve with an amplitude of $0.06 \pm 0.01$ mag
	5.91	T14	Other possible solutions (aliases) are mentioned: 4.76 h and 7.87 h
Spectral slope (%/100 nm)	$19.2 \pm 0.6$	F09	
Density $\rho$ ( $\text{g cm}^{-3}$ )	1.12 / 0.63	T10	Associated with the aforementioned periods (5.9 h & 7.87 h) and sizes, resp.
Bulk density of the system	$1.27^{+0.41}_{-0.44}$	V14	Assuming that Varda and Ilmarë have equal albedo and density values
Varda-Ilmarë ( $\text{g cm}^{-3}$ )	$1.24^{+0.50}_{-0.35}$	G15	Using the aforementioned mass and radius
<b>Varda’s ecliptic orbital elements</b>			
$a$ (AU)	46.046	LS	
$e$	0.140	LS	NIMA ephemeris, see text
$i$ (deg)	21.498	LS	
<b>Ilmarë’s orbital elements (ref:G15)</b>			
		solution 1	solution 2
$a$ (km)		$4812 \pm 35$	$4805 \pm 35$
$e$		$0.0181 \pm 0.0045$	$0.0247 \pm 0.0048$
Orbital pole (J2000)			
$\alpha_p$ (deg)		$273.0 \pm 1.5$	$229.5 \pm 1.5$
$\delta_p$ (deg)		$-11.0 \pm 1.9$	$4.9 \pm 1.8$

**Notes. References:** T10: Thirouin et al. (2010) – T14: Thirouin et al. (2014) – F09: Fornasier et al. (2009) – V14: Vilenius et al. (2014) – G15: Grundy et al. (2015) – A16: Alvarez-Candal et al. (2016) – LS : NIMA ephemerides <https://lesia.obspm.fr/lucky-star/obj.php?p=426>.

<sup>(a)</sup> Vilenius et al. (2014) define the radiometric (area-equivalent) effective diameter of a binary system as  $D = \sqrt{D_1^2 + D_2^2}$ , where  $D_1$  and  $D_2$  are the primary’s and secondary’s diameters, respectively. <sup>(b)</sup> This assumes a linear trend of the phase curves and considers a magnitude variability that is due to the rotational light-curve.

### 2.3. Varda’s rotational period

Thirouin et al. (2010, 2014) reported on broadband CCD photometric observations carried out between 2006 and 2013 using several telescopes for the Varda-Ilmarë system. They give three possible solutions for Varda’s rotation period (Table 1). Although their analysis of the low-amplitude ( $0.06 \pm 0.01$  mag) single-peaked light-curve favours the 5.91 h period, the study shows the existence of two aliases at 4.76 h and 7.87 h that cannot be discarded. Note that all these periods are much smaller than the mutual orbit’s period, which is estimated at  $\sim 138$  h (5.75 days), see Grundy et al. (2015). These authors compiled all the photometric data from Thirouin et al. (2010, 2014) and re-evaluated the associated Lomb periodogramme (Lomb 1976; Press et al. 1992), attempting to identify frequencies that could/would be expected for tidally locked components in the system. The results were inconclusive.

### 3. Varda’s ephemeris & the occultation’s prediction

Occultations by TNOs provide valuable opportunities to measure their physical characteristics from ground-based observations. Huge efforts are dedicated to the predictions of events (Assafin et al. 2012; Camargo et al. 2014; Desmars et al. 2015)). The second release of *Gaia* stellar catalogue (Gaia Collaboration et al. 2016, 2018) ensures an accuracy to the tenth of milli-arcsec (mas), thus most of the uncertainty in the prediction resides in the ephemerides of the TNOs.

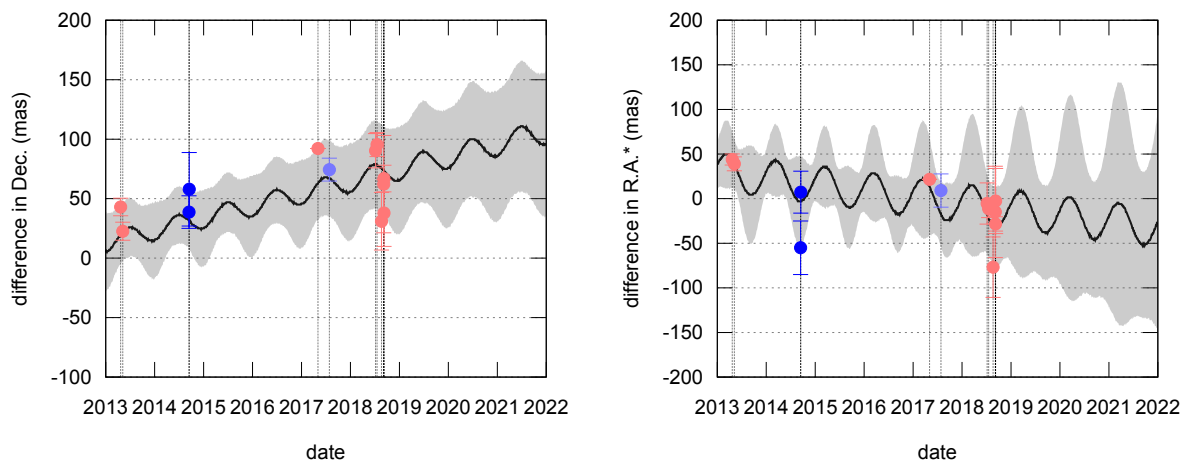


Fig. 1: Difference between NIMAv6 and JPL7 in DEC (declination, left) and R.A.\* (right ascension weighted by  $\cos \delta$ , right) over the time interval 2013-2022. Each dot represents the mean residual and the standard deviation of one night of observations. Dark blue points indicate data reduced with the WFI (Wide Field Imager) catalogue (see text), light blue points are for data reduced with *Gaia*-DR1 and light red points are for data reduced with *Gaia*-DR2. The continuous black line represents the best-fitting curve to these data, whereas the grey shaded area represents the  $1-\sigma$  uncertainty of the NIMAv6 ephemeris (<https://lesia.obspm.fr/lucky-star/obj.php?p=46>).

Table 2: Occultation’s circumstances.

<b>Occultation prediction from NIMAv6</b>	
Date & Time at geocentric close approach	September 10 <sup>th</sup> , 2018, 03:38:37 $\pm$ 117 s UT
Uncertainty on Varda’s position (RA and DEC)	$\Delta\alpha \cos(\delta) = 43.4$ mas, $\Delta\delta = 37.4$ mas
Along-track uncertainty	1274 km (37.6 mas)
Across-track uncertainty	1460 km (43.1 mas)
Geocentric shadow velocity	10.86 km s <sup>-1</sup>
Maximum expected duration and magnitude drop	66.7 s, 5.6 mag
Geocentric closest approach Varda-star	(85 $\pm$ 43) mas
<b>Occulted Star (from <i>Gaia</i>-DR2)</b>	
Star source ID (stellar catalogue)	4367203805493754752
Geocentric star position (J2000) at the epoch	$\alpha = 17 : 18 : 25.12481 \pm 0.2$ mas, $\delta = -02 : 05 : 14.4282 \pm 0.1$ mas
G-mag / RP magnitude (mag)	14.7 / 13.8
Stellar diameter projected at Varda’s distance	0.82 km
<b>Varda at occultation epoch</b>	
Geocentric distance $\Delta$	46.6335 AU
Apparent diameter (physical diameter)	21.4 mas (724 km)
Apparent V. magnitude	20.3

To get the most accurate ephemeris, regular astrometric observations are performed by our team in different observatories (ESO, Observatório do Pico dos Dias, Sierra Nevada, etc). The astrometric reduction of these observations makes use of the *Gaia* catalogue, while orbits and ephemerides are obtained using the NIMA procedure (Desmars et al. 2015).

For the prediction of this occultation, astrometric observations from MPC (1980-2018), ESO (2013), Observatório Pico dos Dias (2014, 2017, 2018) and Sierra Nevada (2018) were used to derive NIMAv6 solution of Varda’s orbit. As the position of Ilmarë around Varda is unknown, photo-centre and barycentre of Varda’s system are assumed to be blended with Varda’s centre in the NIMA orbit determination.

Figure 1 presents a comparison between the NIMAv6 and JPL7 solutions in right ascension (weighted by  $\cos \delta$ ) and in declination between 2013 and 2022. Residuals of observations from our survey are represented by mean points with their standard deviations as error bars (one point for observations during the same night). Dark blue points indicate data reduced with the WFI catalogue (Assafin et al. 2012; Camargo et al. 2014), light blue points are for data reduced with *Gaia*-DR1 and light red points are for data reduced with *Gaia*-DR2. NIMA also allows an estimation of the orbit uncertainty ( $1-\sigma$ ) represented in grey area.

Using NIMAv6 solution for the ephemeris and *Gaia*-DR2 stellar position, the predicted geocentric mid-time for the occultation was on September 10<sup>th</sup>, 2018 at 03:38:37 UT ( $\pm$ 117 sec). Table 2 provides the circumstances of the occultation and Fig. 2 shows the prediction map.

This occultation was also predicted by RECON<sup>3</sup> using ephemeris based only on Minor Planet Center data without additional astrometric positions. The predicted path<sup>4</sup>, shifted to the West ( $\sim 1500$  km) compared to Lucky Star prediction, highlights the importance of adding new astrometry and doing specific work to support the orbit fitting beyond automatic tools. Our new astrometric positions for Varda are provided in the appendix as well as a supplementary material in the form of an ASCII file.

The final prediction was made available to observers through the Lucky Star webpage, the RECON webpage as well as Occult Watcher<sup>5</sup>.

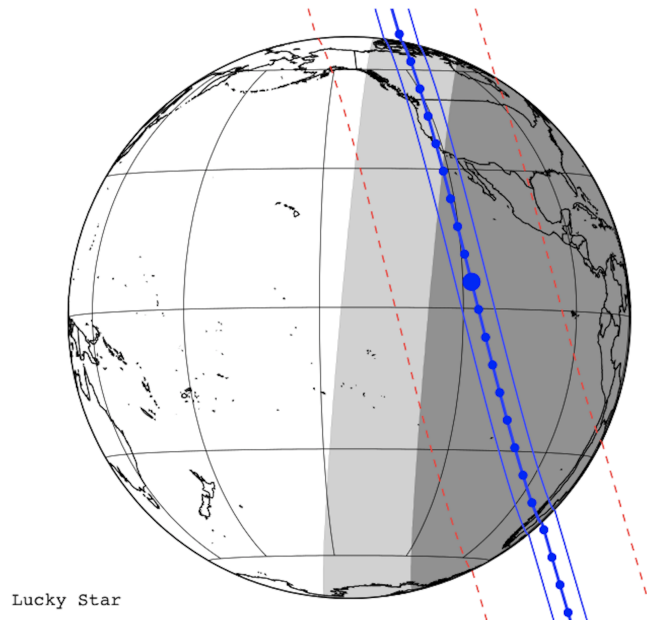


Fig. 2: Predicted shadow track for the September 10<sup>th</sup>, 2018 Varda occultation, see parameters in Table 2. Dark-grey, light-grey and clear areas are in the night, twilight and daytime, respectively. Varda’s shadow is delimited by the continuous blue lines. It moves from north to south, each bullet corresponding to one-minute intervals, the largest bullet corresponding to geocentric closest approach. The red dashed lines show the  $1\text{-}\sigma$  path uncertainty, largely dominated by the uncertainties of the NIMAv6 ephemeris (Fig. 1) when compared to the star’s position (Table 2).

## 4. Data analysis

Observations were performed at thirteen different stations in the USA (see acronyms in Table 3). The observers were organised in eight RECON teams as well as five IOTA<sup>6</sup> (non-RECON) teams. The BDR team used a QHY174M-GPS, while all the other stations used IOTA-VTI timestamp. All other relevant information regarding the observing circumstances are summarised in Table 3.

### 4.1. Occultation light-curves

Eleven stations recorded data during the occultation, five of which (TWF, MHV, YMA, CAR, and FLO) reported positive detections. Differential aperture photometry was used to obtain the occultation light-curves, using the Platform for Reduction of Astronomical Images Automatically (PRAIA, Assafin et al. 2011). The light-curves from the five aforementioned stations are shown in Fig. 3; their photometric measurements are provided as supplementary material to this paper. Fig. 3 presents these light-curves to which we have applied a manual offset in flux and centred at their respective mid-occultation times, for the sake of legibility.

### 4.2. Ingress and egress timings

The start (ingress) and end (egress) times of the occultation were determined by fitting each event by a sharp opaque edge model, after convolution by (1) Fresnel diffraction, (2) finite CCD bandwidth, (3) finite stellar diameter, and (4) finite integration time (see Braga-Ribas et al. 2013; Ortiz et al. 2017 for details).

<sup>3</sup> Research and Education Collaborative Occultation Network (Buie & Keller 2016)

<sup>4</sup> [https://www.boulder.swri.edu/~buie/recon/events/174567\\_180910\\_0154895.html](https://www.boulder.swri.edu/~buie/recon/events/174567_180910_0154895.html)

<sup>5</sup> <https://www.occultwatcher.net/>

<sup>6</sup> The International Occultation Timing Association has had a four decade old mission to observe and record eclipses of stars by minor planets and other bodies. Since the first announced observation there have been thousands of successful observations. In the past decade digital video records have been created with time sensitivities to .003 seconds. IOTA contributors did not receive funding and participated in this study on a voluntary basis.

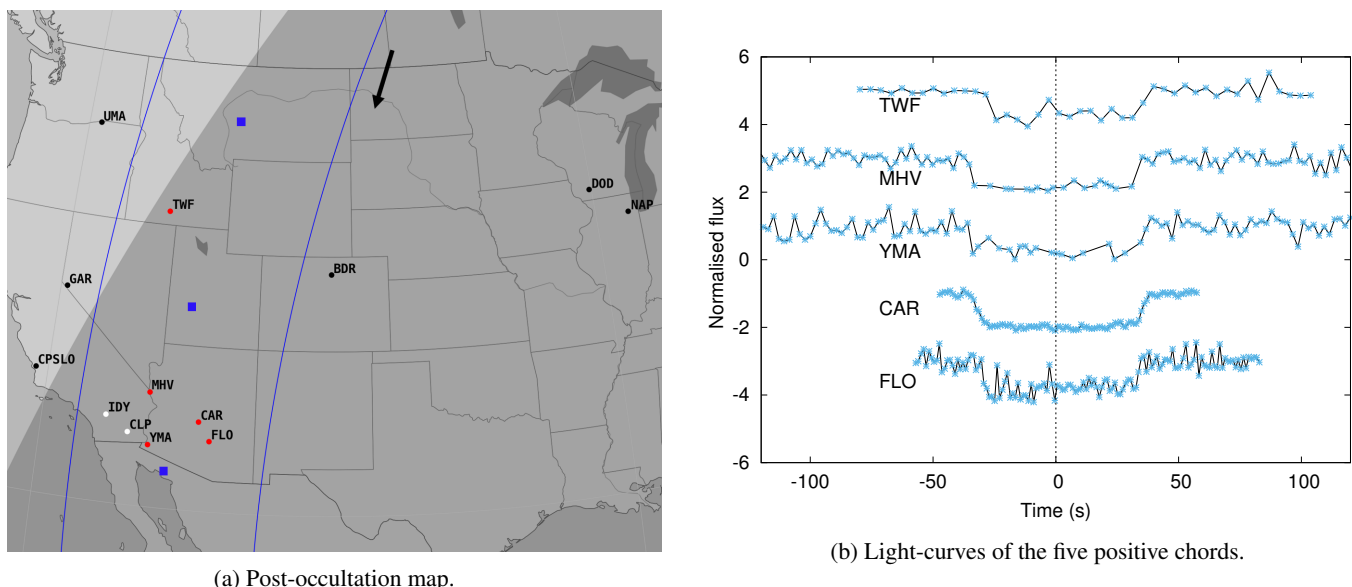


Fig. 3: Sub-figure 3a shows the post-occultation map for the Sept. 10<sup>th</sup>, 2018 stellar occultation by Varda. Blue lines represent the object's projected equivalent diameter, whereas blue squares represent the position of the body's centre (every minute), the northern-most dot corresponding to 03:33:02.934 UTC. The direction of the shadow is shown by the black arrow at the top centre of the figure. The red pins/ black pins on the map represent the sites that reported +ve / -ve observations, whereas the white ones are for the (NDR - no data recorded) stations that experienced technical issues preventing them from recording the occultation (cf. Table 3). Sub-figure 3b shows the five occultations detected at the TWF, MHV, YMA, CAR, and FLO stations (from the western-most to the eastern-most on the Sky-plane cf. Figure 6). Each light-curve has been normalised between 0 (Varda's flux) and 1 (unocculted star + Varda's fluxes). For the sake of legibility, each light-curve has been centred at mid-chord time for each chord and a manual offset in flux has been applied. The associated data to the normalised, non-centred light curves is provided as supplementary material to the paper.

Fresnel diffraction operates over the scale  $F = \sqrt{\lambda\Delta/2}$ , where  $\lambda$  is the wavelength of observation and  $\Delta$  the geocentric distance of the object. From Table 2 we obtain  $F \sim 0.5$  km in visible wavelengths. We estimate the stellar diameter to 0.8 km projected at Varda's distance, using B, V, K magnitudes of 15.61, 14.32, 11.704 for the star (NOMAD catalogue, Zacharias et al. (2004)), respectively, using van Belle (1999)'s formulae and Ochsenbein et al. (2000)<sup>7</sup>. Given the geocentric shadow velocity of  $10.86 \text{ km s}^{-1}$  and exposure times  $> 1$  s at all stations (see Tables 2 and 3), the main cause of light-curve smoothing is the finite integration time, and not Fresnel diffraction or stellar diameter. However, the CAR station required further analysis, as an instrumental effect caused a smoothing of the light-curves over several data points (see Fig 5), resulting in gradual ingress and egress, see discussion below. The occultation timings are obtained by minimising the classical  $\chi^2$  function, using the same procedures as described in Sicardy et al. (2011). The best-fitting functions are displayed in Fig. 4 and the resulting chord details are listed in Table 4.

#### 4.3. The case of the CAR station

The CAR station light-curve (Fig. 5) shows a gradual ingress and egress of the star; both the ingress and egress extend over more than 5 data points, i.e. more than five seconds. Two scenarios were considered to explain this behaviour, (i) a Varda atmosphere or (ii) an instrumental effect.

In case (i), a ray-tracing code was considered. It uses a nitrogen atmosphere with a temperature profile comparable to that of Pluto, with a rapid increase of temperature just above the surface that connects to an upper isothermal branch at  $\sim 100$  K. Then a surface pressure and temperature of  $\sim 1 \mu\text{bar}$  and 38 K, respectively reproduces the profile of Fig. 5. Meanwhile, the four other stations (TWF, MHV, YMA, and FLO) do not have sufficient SNR and/or time resolution to test this model.

Case (ii): a closer examination of the CAR images revealed a slow motion of the stellar images. During ingress, the occulted star fades away but its image no longer moves on the array, while the other sources continue to move clearly, indicating an instrumental effect (more details are given in Appendix B). To account for the aforementioned effect, we have added in the modelling of the occultation light-curve a non-instantaneous instrumental response. More precisely, we have considered two possibilities for the response to an instantaneous light pulse:

- in the first case, we assume a simplified response that decays linearly over a time interval of  $\Delta t_{\text{resp}}$ . Exploring values of  $\Delta t_{\text{resp}}$  between 0 and 10 seconds with steps of 0.01s, the occultation timings and the optimal  $\Delta t_{\text{resp}}$  values are obtained by minimising the classical  $\chi^2$  function as done for the other light-curves. We find the best (and satisfactory) simultaneous fit to the ingress and egress for  $\Delta t_{\text{resp}} = 6.58_{-0.52}^{+0.63}$  s. (Fig. 5a).

<sup>7</sup> <http://vizier.u-strasbg.fr/viz-bin/VizieR>

Table 3: Observing circumstances of the 13 stations: 5 positive (+ve) chords, 6 negatives (-ve) and 2 NDR (no data recorded) stations that experienced of technical issues.

Site	Topocentric coordinates		Elevation (m)	Telescope's diameter (cm)	Camera	Exposure <sup>a</sup> time (s)	Detection status	Observers
	Longitude W	Latitude N						
CPSLO*	120 39 36.0	35 18 01.8	119	28	Mallincam 428	2.135	-ve	M. Kehrlı, C. Spencer, & M. Keidel
GAR*	119 40 20.3	38 53 23.5	1502	30	Watec 910HX	1.068	-ve	J. Bardecker
UMA*	119 17 53.9	45 55 19.9	140	30	Watec 910HX	1.068	-ve	T. George
IDY*	116 42 42.0	33 44 03.0	1639	30.5	Mallincam 428	none	NDR	K. McArdle
CLP*	115 31 28.0	33 07 30.0	-56	28	Mallincam 428	none	NDR	<sup>(b)</sup>
MHV*	114 35 48.9	35 01 54.1	184	28	Mallincam 428	2.135	+ve	J. White
TWF	114 28 13.1	42 35 01.9	1133	60	Watec 120N+	4.271	+ve	C.J. Anderson
YMA*	114 26 10.5	32 39 34.0	97	28	Mallincam 428	2.135	+ve	K. Conway, & D. Conway
CAR	111 57 07.9	33 48 42.9	654	28	Watec 910HX	1.068	+ve	P. D. Maley
FLO	111 21 00.6	33 00 54.3	484	28	Watec 120N+	1.068	+ve	W. Thomas
BDR*	105 09 46.8	40 15 09.0	1587	28	QHY174M	0.5	-ve	M. Buie, J. Keller, & S. Haley
DOD	090 08 31.1	42 57 36.9	390	30.5	Watec 910HX	1.068	-ve	D. Oesper
NAP	088 06 59.7	41 45 32.5	230	35	QHY174M	1	-ve	B. Dunford

**Notes.** \* The sites annotated with a (\*) belong to the RECON network (Buie & Keller 2016).

<sup>(a)</sup> The exposure time is equal to the cycle time.

<sup>(b)</sup> CLP observers: A. McCandless, K. McCandless, X. Banaga, A. Carrillo, K. Hudson, D. Laguna, C. Lara, E. Self, S. Valdez, L. Torres, M. Garcia, J. Bustos, J. Cota.

Acronyms: **CPSLO**: California Polytechnic State University, San Luis Obispo, California; **GAR**: Gardnerville, Nevada; **UMA**: Umatilla, Oregon; **IDY**: Idyllwild, California; **CLP**: Calipatria, California; **MHV**: Mohave Valley, Arizona; **TWF**: Twin Falls, Idaho; **YMA**: Yuma, Arizona; **CAR**: Carefree, Arizona; **FLO**: Florence, Arizona; **BDR**: Boulder, Colorado; **DOD**: Dodgeville, Wisconsin, and **NAP**: Naperville, Illinois.

b. in the second case, we assume an (RC) electronic filter response ( $e^{-t/\tau}$ , where  $\tau$  is the capacitor's time constant) convolved with a rectangular function response that accounts for the finite integration time (cf. Table 3). We explore  $\tau$  values in the interval [0,10] seconds with a step of 0.015 s. The occultation timings and the optimal  $\tau$  values timings are obtained by minimising the classical  $\chi^2$  function as done for the other light-curves. We find the best (and satisfactory) simultaneous fit to both ingress and egress for  $\tau = 3.21 \pm 0.45$  s (Fig 5b).

The resulting ingress and egress times obtained by the two methods agree at the 1- $\sigma$  confidence level. However, further analysis of the post-occultation data (cf. Appendix B) motivated our choice of an electrical RC filter (case b above). At last, the overall uncertainty in the timing of this chord is mainly ( $\sim 60\%$ ) due to the uncertainty in the modelling of the (unknown) instrumental response. The gradual ingress and egress is clearly due to an instrumental effect.

The resulting egress and ingress timings as well as the duration and length of the chords at the five positive stations are listed in Table 4.

Table 4: Signal-to-noise ratio (SNR) per data point outside the occultation, and results of the fits displayed in Figs. 4 and 5 (timings, durations and lengths of the chords).

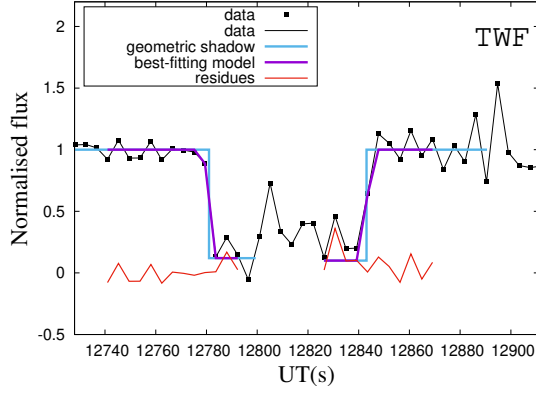
Site	Ingress time (UT hh:mm:ss.s)	Egress time (UT hh:mm:ss.s)	Chord's duration (s)	Chord's length (km)	SNR per data point
TWF	03:32:57.10 $\pm$ 0.60	03:33:58.83 $\pm$ 0.60	61.73 $\pm$ 0.85	670.4 $\pm$ 9.2	6.7
MHV	03:33:56.99 $\pm$ 0.76	03:35:05.27 $\pm$ 0.30	68.28 $\pm$ 0.82	741.5 $\pm$ 8.9	5.7
YMA	03:34:17.10 $\pm$ 0.60	03:35:26.39 $\pm$ 0.59	69.29 $\pm$ 0.84	752.5 $\pm$ 9.1	3.7
CAR	03:34:12.39 $\pm$ 0.47	03:35:19.52 $\pm$ 0.47	67.13 $\pm$ 0.66	729.0 $\pm$ 7.2	20
FLO	03:34:23.30 $\pm$ 0.13	03:35:26.75 $\pm$ 0.15	63.45 $\pm$ 0.20	689.1 $\pm$ 2.2	4.8

## 5. Results & Discussions

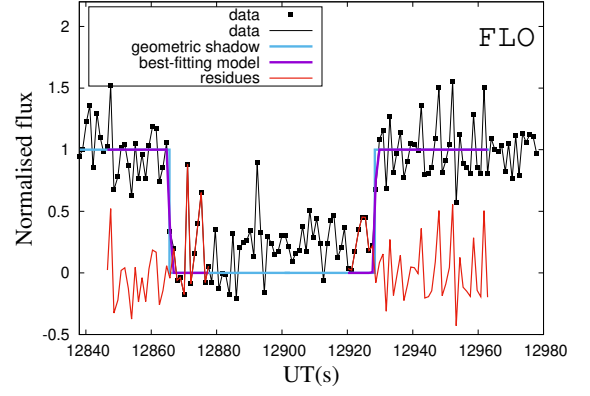
### 5.1. Elliptical fit to Varda's limb

Given that Varda's diameter is larger than 500 km (cf. Table 1), it is reasonable to assume that its limb is close to elliptical due to hydrostatic equilibrium (Tancredi & Favre 2008). Therefore, following the same procedures as in previous works (Braga-Ribas et al. 2013, 2014; Benedetti-Rossi et al. 2016, 2019; Dias-Oliveira et al. 2017; Ortiz et al. 2017), we fitted an ellipse to the chord extremities. The limb fitting depends on five adjustable parameters:

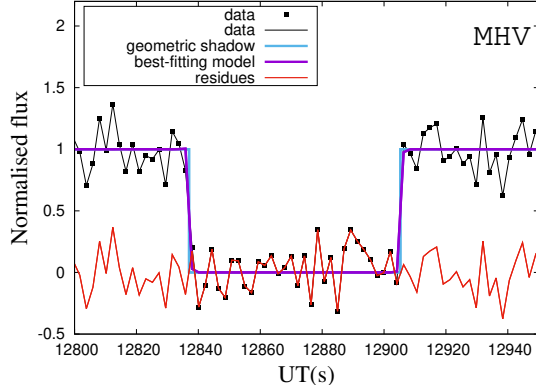




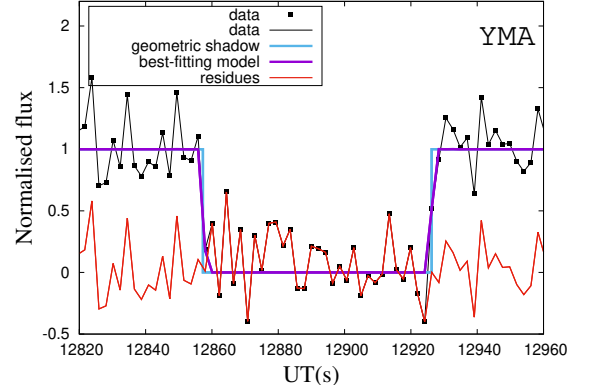
(a) Fit to ingress and egress for the TWF station.



(b) Fit to ingress and egress for the FLO station.



(c) Fit to ingress and egress for the MHV station.



(d) Fit to ingress and egress for the YMA station.

Fig. 4: Fit to ingress and egress at four of the stations.

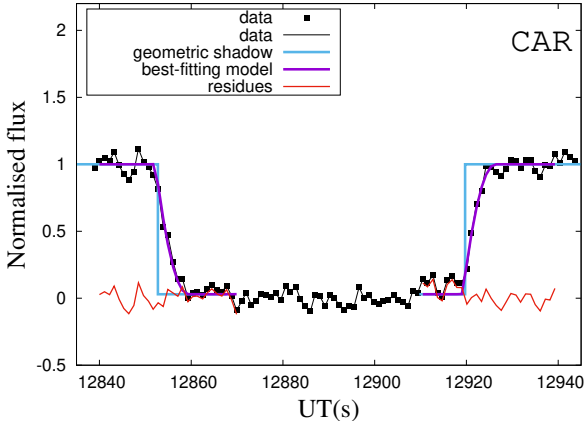
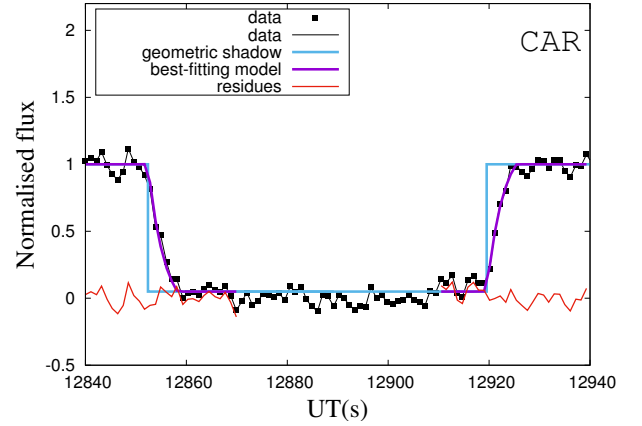

(a) Assuming a response that decays linearly over a time interval  $\Delta t_{\text{resp}} = 6.58$  s (see text).

(b) assuming an (RC) electronic filter response with a time constant  $\tau = 3.21$  s (see text).

Fig. 5: Fitting of the CAR station chord. Note the gradual ingress and egress caused by the instrumental effect, see text for details.

- i. The centre of the ellipse,  $(f_c, g_c)$ , that measures the offsets in  $\alpha$  and  $\delta$  to apply (eastwards and northwards, respectively) to the adopted ephemeris (NIMAv6), assuming the star position of Table 2;
- ii. The apparent semi-major axis  $a'$ ;
- iii. The apparent oblateness  $\epsilon' = (a' - c')/a'$ , where  $c'$  is the apparent semi-minor axis;
- iv. The position angle  $P'$  of the apparent semi-minor axis  $c'$ , measured eastwards from Celestial North.

These parameters are varied in wide ranges to find the best-fitting limb. More precisely, we explore:  $-90^\circ < P' < 90^\circ$  with steps of  $1^\circ$ ,  $0 < \epsilon' < 0.5$  with steps of 0.005, and  $350 \text{ km} < a' < 450 \text{ km}$  with 1 km steps. For each value of  $P'$ ,  $\epsilon'$  and  $a'$ , we determine the best-fitting ellipse by adjusting the centre  $(f_c, g_c)$ . This best-fitting limb is obtained by minimising the function  $\chi^2 = \sum_{i=1}^{N=6} (r_i - r_{\text{ell},i})^2 / \sigma_i^2$ , where  $r_i$ ,  $r_{\text{ell},i}$  the radial distance of the  $i^{\text{th}}$  occultation point to the shadow's centre and to the elliptical



limb model, respectively.  $\sigma_i$  is the radial uncertainty ( $1\sigma$  level) stemming from the occultation's timing uncertainties (Table 4). The  $\chi^2$  value is based on the radial residual of the actual limb relative to the limb model. The associated error bar on each data point is then the timing uncertainty in the direction of the chord multiplied by the (radial) velocity of the star with respect to the centre of the body. As such, it is fully consistent with the approach that would minimise the residuals along the chords. Admittedly, this equivalence of methods works as long as the limb remains close to circular and none of the chords are close to grazing, which is the case here.

We define the value of  $\chi^2$  per degree of freedom (or unbiased  $\chi^2$ ) by  $\chi_{\text{pdf}}^2 = \chi^2/(N - M)$ , where  $N = 10$  is the number of data points and  $M = 5$  is the number of adjustable parameters. Fig. 6 displays the results of those fits and Table 5 provides the best-fitting adjusted parameters. The expected minimum value of  $\chi_{\text{pdf}}^2$  for a satisfactory fit is  $\chi_{\text{minpdf}}^2 = \frac{N-M}{M} = 1$ , which is the case from Table 5, noted  $\chi_{\text{pdf}}^2 = 1.32$ .

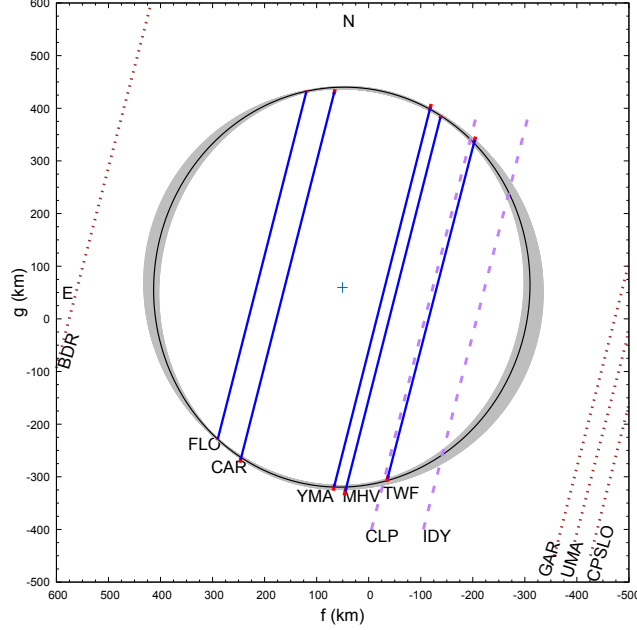


Fig. 6: The blue lines are the occultation chords derived from Table 4, while the red segments are the uncertainties at the chords extremities. The black ellipse is the best-fitting solution, whose parameters are given in Table 5. The grey area shows all the solutions that are found to within a  $1\text{-}\sigma$  level from the best fitting ellipse, i.e. corresponding to  $\chi^2 < \chi_{\text{min}}^2 + 1$ . The purple dashed lines show the projections onto the sky from the two NDR stations (cf. Table 3), whereas the brown dotted lines show the projections from the near miss stations (cf. Figure 3a).

Table 5: Parameters of the elliptic fit to the limb.

Apparent semi-major axis	$a' = (381 \pm 3)$ km
Apparent oblateness	$\epsilon' = 0.043 \pm 0.036$
Equivalent Radius <sup>(a)</sup>	$R'_{\text{equiv}} = (373 \pm 8)$ km
Geometric albedo <sup>(b)</sup>	$p_v = 0.097 \pm 0.004$
Position angle	$P' = (113 \pm 34)$ deg
Best fit $\chi_{\text{pdf}}^2$ <sup>(d)</sup>	$\chi_{\text{pdf}}^2 = 1.32$
Varda's J2000 geocentric position <sup>(c)</sup>	on Sept. 10 <sup>th</sup> , 2018 at 03:34:00 UT
RA	$17\ 22\ 51.853657 \pm 0.218$ mas
DEC	$-02\ 03\ 47.705738 \pm 0.176$ mas

**Notes.** <sup>(a)</sup> The apparent area-equivalent radius is  $R'_{\text{equiv}} = \sqrt{a'c'} = a' \sqrt{1 - \epsilon'}$ , where  $c'$  is the apparent polar radius. <sup>(b)</sup> We do not know Varda's rotational phase at the epoch of the occultation; therefore we cannot account for the peak-to-peak  $\Delta\text{mag} = 0.06$  mag amplitude of Varda's rotational light-curve (Thirouin et al. 2010). This adds an additional uncertainty of  $\pm 0.03$  on  $p$ . <sup>(c)</sup> The associated centre  $(f_c, g_c) = (50.49 \pm 3.29, 59.43 \pm 1.81)$  km of the ellipse (Fig. 6) measures the offsets in  $\alpha$  and  $\delta$  to apply to the adopted NIMAv6 ephemeris, which yields to this new astrometric position. <sup>(d)</sup> The calculation of  $\chi_{\text{pdf}}^2$  is explained in the text.

In our paper, the  $1\text{-}\sigma$  error bars on each fitted parameter stem from their respective *marginal probabilities*, and more precisely, their 68.3% confidence level values, *without consideration of the other adjusted parameters*. These domains are bound by the  $\chi^2 < \chi_{\text{min}}^2 + 1$  criterion. This same approach was adopted in (Braga-Ribas et al. 2013, 2014; Benedetti-Rossi et al. 2016, 2019;

Dias-Oliveira et al. 2017; Ortiz et al. 2017). The  $\chi^2 < \chi_{min}^2 + 1$  limit corresponds to confidence limit for one free parameter, while considering simultaneously all five free parameters, the formal  $1 - \sigma$  confidence value for  $\chi^2$  would write  $\chi^2 < \chi_{min}^2 + 5.89$  (this is not the adopted approach here).

## 5.2. Size, shape, geometric albedo, and density of Varda

### 5.2.1. The geometric albedo $p_V$

We use the equivalent radius  $R'_{equiv}$  given in Table 5 and Varda's visual absolute magnitude  $H_V$  from the literature to derive the associated geometric albedo for Varda. The absolute magnitude given in the literature is that of the system Varda-Ilmarë (cf. Table 1). Moreover, as mentioned in Sect. 2.2, Grundy et al. (2015) have measured a difference in the visible magnitude between the two components  $\Delta m = (1.734 \pm 0.042)$  mag. It follows that Varda's absolute magnitude is  $H_V = 3.81 \pm 0.01$ . Using this latter value of the absolute magnitude, we derive the geometric albedo of Varda<sup>8</sup>,  $p = 0.097 \pm 0.004$ .

The geometric albedo value that we derive is consistent with but more accurate than the value from radiometric measurements  $p_V = 0.102^{+0.024}_{-0.020}$  of Vilenius et al. (2014). This shows that Varda is about as dark as the binary TNO 2003 AZ<sub>84</sub> (Dias-Oliveira et al. 2017).

Moreover, recent thermal emission data of the Varda-Ilmarë system observed with ALMA has shown that the ratio of the primary's radius to the secondary's is  $\sim 2.10$  (Moulet, A. & Lellouch, E., priv. communication May 2020). Given the equivalent radius of Varda (cf. Table 5), we derive an equivalent radius of  $\sim 178$  km for Ilmarë, about 15 km larger than Grundy et al. (2015)'s value. Furthermore, using a difference  $\Delta m = 1.734$  mag between the primary and the secondary implies that the albedo of Ilmarë is  $\sim 0.89$  times that of Varda, i.e.  $\sim 0.085$ .

### 5.2.2. Geometrical considerations

We now use the 2D limb fit obtained above to constrain Varda's 3D shape. To do so, simplified assumptions must be made: Varda is an oblate, axisymmetric spheroid with equatorial radius ( $a$ ), polar radius ( $c$ ), and true oblateness  $\epsilon = (a - c)/a$ . This choice is based on the small amplitude of Varda's rotational light-curve ( $\Delta mag = (0.06 \pm 0.01)$  mag,<sup>9</sup> see Table 1) which favours a spheroid solution over a non-axisymmetric, triaxial ellipsoid (Thirouin et al. 2014), i.e. the flux variations caused by albedo variegation.

The axisymmetric assumption leads to  $a = a'$ . Moreover, the apparent oblateness  $\epsilon'$  is related to the true oblateness  $\epsilon$  by the classical formula  $c'^2 = a^2 \sin^2 B + c^2 \cos^2 B$  ( $c'$  is the apparent polar radius), i.e.

$$(1 - \epsilon')^2 = \sin^2 B + (1 - \epsilon)^2 \cos^2 B, \quad (1)$$

where  $B$  is the planeto-centric sub-observer latitude, such that  $B = 0^\circ$  ( $B = 90^\circ$ , resp.) corresponds to equator-on (pole-on, resp.) viewing geometry.

The density  $\rho$  is then derived from the mass  $M$  divided by the volume  $3a^2c/4\pi$ . From  $c = a(1 - \epsilon)$  and Eq. 1, we obtain

$$\rho = \frac{3M}{4\pi a'^3} \frac{\cos B}{\sqrt{(1 - \epsilon')^2 - \sin^2 B}}. \quad (2)$$

The mass  $M$  is an observable quantity, while  $a'$  and  $\epsilon'$  are derived in the previous sub-section (see Table 5). Grundy et al. 2015 give the system's mass (Varda plus Ilmarë)  $M = (2.664 \pm 0.064) \times 10^{22}$  kg, where Varda accounts for 92% of the system's mass. We adopt here a mass of  $M = (2.45 \pm 0.06) 10^{22}$  kg for Varda alone. As  $B$  is a priori unknown, Eqs. 1 and 2 define a parametric curve  $\epsilon(\rho)$  travelled as  $B$  varies from 0 (the equator-on geometry with minimum possible value of  $\epsilon = \epsilon'$ ), to its maximum value  $\arcsin(1 - \epsilon')$ , corresponding to a completely (and unrealistic) flattened object, i.e.  $\epsilon = 1$ . The function  $\epsilon(\rho)$  is plotted in Fig. 7 as the light-blue dashed line. The uncertainty in  $\epsilon'$  causes a displacement of a given point  $\rho(\epsilon)$  along this same curve, while the uncertainties in  $M$  and  $a'$  cause a transverse relative uncertainty in  $\rho$  of:

$$\left(\frac{\delta\rho}{\rho}\right)^2 = \left(\frac{\delta M}{M}\right)^2 + \left(3\frac{\delta a'}{a'}\right)^2, \quad (3)$$

since  $M$  and  $a'$  are determined independently. The resulting error domain for  $\rho$  is delimited by the light-blue continuous lines in Fig. 7. The minimum density provided by the spheroid model is  $\rho \sim 1.16 \pm 0.04$  g cm<sup>-3</sup>, up to an infinite value at  $B = \arcsin(1 - \epsilon') \sim 73^\circ$ , corresponding to a flat object with  $\epsilon = 1$ .

### 5.2.3. MacLaurin solutions

We now go a step further, assuming that Varda is homogeneous and in hydrostatic equilibrium. This implies that Varda is either a MacLaurin spheroid, or a Jacobi triaxial ellipsoid (Chandrasekhar 1987). Note that with a typical equatorial radius of more than

<sup>8</sup> Using  $p = (AU_{km}/R_{equiv})^2 10^{0.4(H_\odot - H)}$ . Where  $R_{equiv}$  is expressed in kilometres,  $H$  and  $H_\odot = -26.74$  are the visual absolute magnitudes of Varda and the Sun, respectively, and  $AU_{km} = 149597870.7$  (Sicardy et al. 2011, supplementary information).

<sup>9</sup> If we were to consider Varda (alone) with no satellite, the light-curve's amplitude will slightly increase (as the difference in magnitude between the two components is  $\Delta m = 1.734$ ) to  $\sim 0.07$ , and our assumptions would still be valid.

380 km (Table 5) and from its derived density (see below), Varda qualifies as a candidate for being a dwarf planet, i.e. a body in hydrostatic equilibrium (Tancredi & Favre 2008).

As mentioned earlier, an axisymmetric spheroid (here, a MacLaurin solution) is preferred over a triaxial ellipsoid (a Jacobi solution). In this case, the density  $\rho$  of the body is related to its spin frequency  $\omega = 2\pi/T_{\text{rot}}$  (where  $T_{\text{rot}}$  is the rotational period) and its true oblateness  $\epsilon$  by

$$\frac{\pi G \rho}{\omega^2} = \frac{\sin^2(\psi) \tan(\psi)}{2\psi[2 + \cos(2\psi)] - 3 \sin(2\psi)}, \quad (4)$$

where  $\cos(\psi) = 1 - \epsilon$  and  $G$  is the gravitational constant (Plummer 1919; Chandrasekhar 1987; Sicardy et al. 2011).

Three possible rotational periods (for single-peaked light-curves) are reported in the literature (see Section 2.3): 4.76 h, 5.91 h (the most probable, according to the authors), and 7.87 h. The resulting MacLaurin curves  $\epsilon$  vs.  $\rho$  are shown in Fig. 7 as purple, green and red curves, respectively. The intersections of the light-blue curve and the MacLaurin solutions in Fig. 7 provide solutions that are consistent with both our occultation results and the MacLaurin hypothesis.

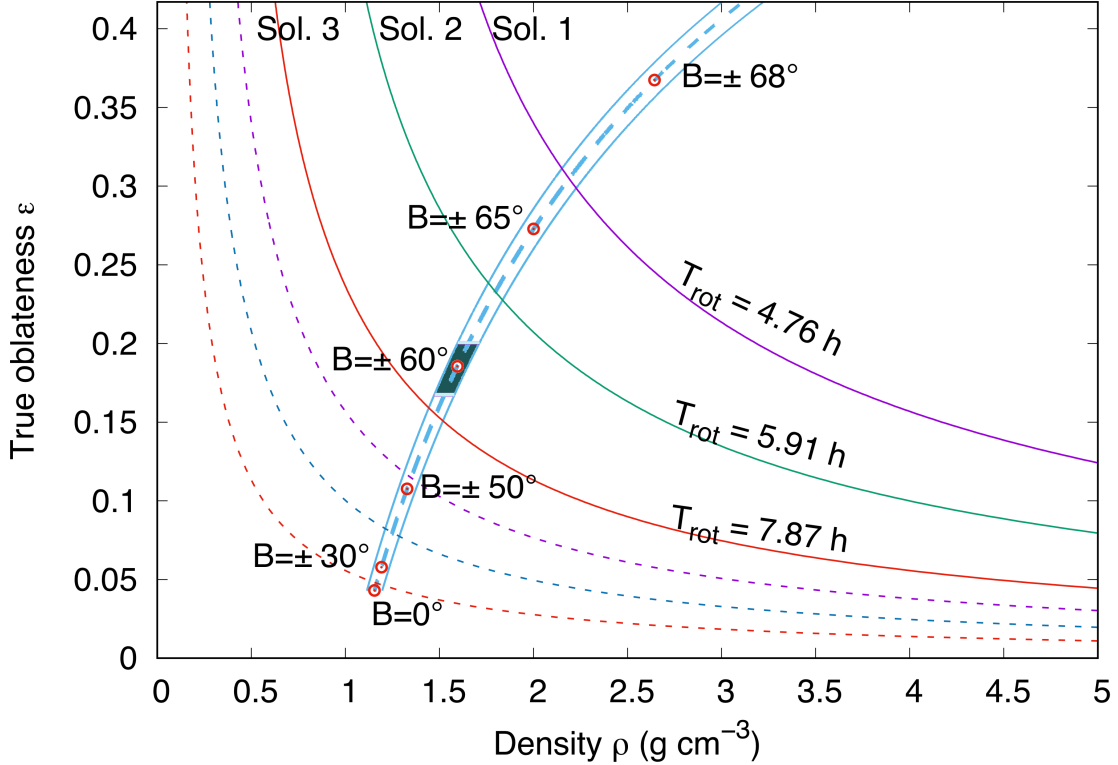


Fig. 7: The dashed light-blue line is Varda’s true oblateness ( $\epsilon$ ) as a function of its density ( $\rho$ ), as derived from our occultation’s results and knowledge of Varda’s mass (see Sect. 5.2.2 for details). The lowest point corresponds to the equator-on geometry ( $B = 0$ ) for Varda, while the upper-most point (outside the figure) corresponds to  $B = \arcsin(1 - \epsilon) \sim 73^\circ$  for  $\epsilon = 1$ . The continuous blue lines to the left and the right of the  $\epsilon(\rho)$  curve delimit the  $1\text{-}\sigma$  uncertainty domain for the density. This domain stems from the uncertainties on  $M$  and  $a'$  (Eq. 3). The MacLaurin solutions (Eq. 4) corresponding to the rotational periods 4.76 h, 5.91 h, and 7.87 h (Thirouin et al. 2014) are shown as solid purple (solution 1), green (solution 2) and red (solution 3) curves, respectively, using Varda’s mass from Sect. 5.2.2. The red circles along the curve  $\epsilon(\rho)$  indicate some planetocentric sub-observer latitudes  $B$ . The shaded region corresponds to one of the possible Ilmarë’s orbit opening angle at epoch,  $B_{\text{open}} = -59.8^{+1.4}_{-1.3}$ . A solution compatible with an equatorial orbit for Ilmarë would be between solutions 2 and 3 (shaded area). For each MacLaurin solution, we plot as dashed lines of same colours the corresponding solutions with the double period, i.e. assuming double-peaked rotational light-curves (see Section 5.2.3 for details).

All possible MacLaurin solutions consistent with our occultation’s results are summarised in Table 6. Solutions 1, 2, and 3 are associated with the 4.71 h, 5.91 h, and 7.87 h rotational periods of the single-peaked light-curves, respectively; while solutions 1bis, 2bis, and 3bis are associated with the respective double periods (i.e. 9.52 h, 11.81 h, and 15.74 h). Although the light-curves associated with these double periods would mean a body with a double-peaked rotational light-curve due to albedo features on opposite sides of the body, these solutions shall not be discarded because of the low-amplitude of the rotational light-curve (see previous sections). This stems from the extremely low-amplitude variability ( $\Delta m < 0.15$  mag), for which distinguishing the period from its double is nearly impossible (Thirouin et al. 2014). Finally, we cannot exclude the existence of a non-axisymmetric, triaxial ellipsoid solution, in particular a Jacobi-type body close to a pole-on orientation (to explain the low peak-to-peak amplitude of the light-curve  $\sim 0.06$  mag).

Table 6: MacLaurin solutions consistent with our occultation results: this table gives the solutions for each one of the three possible periods as well as their respective aliases (annotated with the suffix 'bis')

Rotation period (h)	$T = 4.76$ h (solution 1/ 1bis)	$T = 5.91$ h (solution 2/ 2bis)	$T = 7.87$ h (solution 3/ 3bis)
$\rho$ (g cm <sup>-3</sup> )	$2.18 \pm 0.07 / 1.35 \pm 0.05$	$1.52 \pm 0.05 / 1.25 \pm 0.04$	$1.48 \pm 0.05 / 1.17 \pm 0.04$
$B$ (°)	$\sim 66 / \sim 51$	$\sim 63 / \sim 42$	$\sim 57 / \sim 18$
$\epsilon$	$0.305 \pm 0.038 / 0.115 \pm 0.036$	$0.232 \pm 0.036 / 0.079 \pm 0.044$	$0.154 \pm 0.036 / 0.048 \pm 0.036$

Asides for solution 1 (for which  $T = 4.76$  h), all the others give bulk density values that are consistent with but more accurate than the value  $1.27^{+0.41}_{-0.44}$  g cm<sup>-3</sup> derived from thermal measurements for which equal albedo values and equal densities were assumed for both Varda and Ilmarë (Thirouin et al. 2014). Solution 1 gives a much higher and seemingly unlikely density for this size of object ( $2.18 \pm 0.07$  g cm<sup>-3</sup>), close that of Quaoar. This solution, however, shall not be excluded (see discussion in Sect. 5.3).

A further constraint can be considered by requiring an equatorial orbit for Ilmarë. This may, for example, be expected if Ilmarë resulted from the re-accretion of a collisional disc surrounding Varda after an impact. The opening angle of its orbit,  $B_{\text{open}}$ , can be calculated from the orbit's pole position (Table 1) and Varda's astrometric position at epoch.

We examine here the possibility that Ilmarë moves in the equatorial plane of one of the MacLaurin solutions considered above. Grundy et al. (2015) provide two (mirror-ambiguous) solutions for Ilmarë's orbital pole (Table 1). They yield two possible opening angles for Ilmarë's orbit as seen in the sky plane:  $B_{\text{open}} = -74^{\circ}.0^{+0.4}_{-0.2}$  and  $B_{\text{open}} = -59^{\circ}.8^{+1.4}_{-1.3}$ . The first value is incompatible with all MacLaurin solutions considered here, see Fig. 7. Moreover, it would require an unrealistic high density for Varda,  $\rho > 2.5$  g cm<sup>-3</sup>. In contrast, the second Ilmarë orbital solution (represented by the shaded area in Fig. 7) lies between solutions 2 and 3 in terms of opening angles. Moreover, it provides a position angle for the semi-minor axis of the orbit (as projected in the sky plane) of  $96^{\circ}.2^{+4.0}_{-3.6}$ . This is consistent with the position angle  $P' = (113^{\circ} \pm 34^{\circ})$  of Varda's limb semi-axis (Table 5), and thus, with an equatorial orbit for Ilmarë. This solution has a bulk density and oblateness in the ranges 1.47-1.71 g cm<sup>-3</sup> and 0.16-0.20, respectively (see the light-blue shaded region in Fig. 7).

### 5.3. Discussion

The geometric albedo we derive for Varda ( $p = 0.097 \pm 0.004$ , see Table 5) can be compared to those of other TNOs. The dynamically hot population has a median geometric albedo of  $0.085^{+0.084}_{-0.045}$  (Müller et al. 2020), excluding the Haumea family<sup>10</sup> and dwarf planets, noting that the median geometric albedo for cold classical is  $0.14^{+0.09}_{-0.07}$  (Ibid.). More recently, Müller et al. (2020) provided an overview of TNO physical properties at thermal wavelengths, in particular, for a sample of 26 hot classical TNOs (excluding Makemake, Haumea and its family), with geometric albedo values ranging between 0.032 and 0.310, a median at 0.084, and a mean value at 0.102. Thus, Varda's geometric albedo appears in line with those of other hot classical TNOs.

Our results are based on the assumptions that Varda is an oblate, axisymmetric spheroid with equatorial radius ( $a$ ), polar radius ( $c$ ), and true oblateness  $\epsilon = (a-c)/a$ . The small amplitude of Varda's rotational single-peaked light-curve ( $\Delta\text{mag} = 0.06 \pm 0.01$  mag., see Table 1) favours a spheroid solution over a non-axisymmetric, triaxial ellipsoid, and motivates our search for MacLaurin solutions.

With an equatorial radius of about 380 km, Varda falls into the category of Kuiper Belt Objects (KBOs) that make a transition from small porous objects to dense KBOs, as defined in Bierson & Nimmo (2019). Simulations by those authors show that such a transition rapidly occurs for objects in the radius range 200-500 km. To explain the observed density distribution of the KBOs as a function of size, Bierson & Nimmo (2019) studied a sample of 11 out of the 18 well-known TNBs using a 1D model that couples KBO's thermal evolution with porosity evolution (where primordial porosity is removed over time). They have concluded that the density distributions observed within the KBO populations are mainly a consequence of porosity, rather than mass. They have also defined an input rock mass fraction parameter<sup>11</sup>  $f_m = M_S / (M_S + M_i)$ , where  $M_S$  is the mass of silicates and  $M_i$  the mass of ice. In their model Varda has  $f_m > 70\%$ , close to Pluto's value, and much lower than those of Eris ( $f_m \sim 90\%$ ) and Quaoar ( $f_m \sim 85\%$ ) which are much larger and much denser objects compared to Varda. This confirms that the Solution 1 given ( $\rho = 2.18$  g cm<sup>-3</sup>) in Table 6 cannot be excluded just yet.

To summarise, solutions 1, 2, and 3 are compatible with a spheroid MacLaurin solution, whereas solution 1bis, 2bis, and 3bis would be associated with triaxial ellipsoid shape of Varda. As discussed in sub-section 5.2.3, distinguishing a period from its double is nearly impossible when dealing with low-amplitude light-curves. As an example, one can cite Ceres, whose oblate shape is well-known from stellar occultations (Gomes-Júnior et al. 2015) and the DAWN spacecraft visit (Russell et al. 2016), while it exhibits a low-amplitude double-peaked rotational light curve due to albedo features (Chamberlain et al. 2007). In the trans-neptunian region, Makemake is also a clear example of oblate body with low-amplitude double-peaked light-curve (Hromakina et al. 2019).

If we were to assume Varda as a body with a double-peaked light-curve due to albedo features on opposite sides of the body, we should also consider the double of the aforementioned periods (i.e. 9.52 h, 11.82 h, and 17.74 h, respectively). The associated MacLaurin curves are plotted in figure 7 in purple, blue, and red dashed lines, respectively. The associated density and oblateness values are given in Table 6.

<sup>10</sup> Haumea's family is characterised by high geometric albedo values, with a median  $0.48^{+0.28}_{-0.18}$  (Müller et al. 2020).

<sup>11</sup> This is calibrated with a nominal value of 60% as this gives an object with  $f_m = 70\%$  a density of  $\approx 750$  kg/m<sup>3</sup>.

## 6. Conclusion

This study provides unique constraints on fundamental physical properties of Varda, by refining its size, shape, geometric albedo, and bulk density. It uses the first-ever recorded stellar occultation by the TNO (174567) Varda, observed from several stations in the US on September 10<sup>th</sup>, 2018. This event resulted in five positive chords, from which an elliptical limb-fitting provides an apparent semi-major axis of  $(381 \pm 3)$  km and an apparent oblateness of  $0.043 \pm 0.036$ , respectively, an area-equivalent radius of  $373 \pm 8$  km, and a geometric albedo of  $p_v = 0.097 \pm 0.004$ .

We have derived six possible MacLaurin solutions for Varda, three assuming single-peaked rotational light curves and three assuming the associated respective double-peaked rotational light-curves. The associated density and oblateness values are listed in Table 6.

At this time, we cannot discriminate between these solutions. However, two solutions require our attention: that associated with the most probable period ( $T=5.91$  h) for a spheroid body with a single-peaked light-curve (solution 2:  $\rho = 1.52 \pm 0.05$  g cm<sup>-3</sup> and  $\epsilon = 0.232 \pm 0.036$ ), and its double period ( $T=11.82$  h) for a body with a double-peaked light-curve (solution 2bis:  $\rho = 1.25 \pm 0.04$  g cm<sup>-3</sup> and  $\epsilon = 0.079 \pm 0.044$ ). The relatively high densities derived for Varda ( $>1.5$  g cm<sup>-3</sup>) adopting the MacLaurin solutions 1, 2, and 3 are consistent with low porosity for an object in this size-range.

The gradual ingress and egress observed at one of the stations mimic the effect of an atmosphere, but are actually of an instrumental origin. Such effects could be observed again when using similar setups, so some care is necessary to avoid erroneous interpretations.

From a more general standpoint, Trans-Neptunian Binaries like Varda are good occultation candidates to probe the outer Solar System, because they provide accurate shapes (i.e. volumes) for bodies whose masses are well constrained from the satellite's motion. They provide a wide range of densities, from below that of water ice to that of nearly pure rock. Such occultations constrain the formation scenarii for the Solar System and/or the current internal structure of those bodies.

## 7. Acknowledgment

This campaign was carried out within the "Lucky Star" umbrella that agglomerates the efforts of the Paris, Granada and Rio teams. It is funded by the European Research Council under the European Community's H2020 (2014-2020)/ERC Grant Agreement No. 669416).

The following authors acknowledge the respective CNPq grants: FB-R 309578/2017-5; RV-M 304544/2017-5, 401903/2016-8; J.I.B.C. 308150/2016-3 and 305917/2019-6; MA 427700/2018-3, 310683/2017-3, 473002/2013-2. This study was financed in part by the Coordenação de Aperfeiçoamento de Pessoal de Nível Superior - Brasil (CAPES) - Finance Code 001 and the National Institute of Science and Technology of the e-Universe project (INCT do e-Universo, CNPq grant 465376/2014-2). GBR acknowledges CAPES-FAPERJ/PAPDRJ grant E26/203.173/2016, MA FAPERJ grant E-26/111.488/2013 and ARGJr FAPESP grant 2018/11239-8.

J.L.O., P. S-S, N.M., and R.D. acknowledge financial support from the State Agency for Research of the Spanish MCIU through the "Center of Excellence Severo Ochoa" award for the Instituto de Astrofísica de Andalucía (SEV-2017-0709). P.S-S. acknowledges financial support by the Spanish grant AYA-RTI2018-098657-J-I00 "LEO-SBNAF" (MCIU/AEI/FEDER, UE).

Observations from the RECON network were provided by students, teachers, and community members, including Xavier Banaña, Jesus Bustos, Amanda Carrillo, Dorey W. Conway, Kenneth Conway, Danielle D. Laguna, Andrew E. McCandless, Kaitlin McArdle, and Jared T. White, Jr. The observers listed in this paper are but a small fraction of the total RECON network and their dedication to this project is deeply appreciated. Funding for RECON was provided by grants from NSF AST-1413287, AST-1413072, AST-1848621, and AST-1212159.

This work has made use of data from the European Space Agency (ESA) mission *Gaia* (<https://www.cosmos.esa.int/gaia>), processed by the *Gaia* Data Processing and Analysis Consortium (DPAC, <https://www.cosmos.esa.int/web/gaia/dpac/consortium>). Funding for the DPAC has been provided by national institutions, in particular the institutions participating in the *Gaia* Multilateral Agreement.

This research has made use of the VizieR catalogue access tool, CDS, Strasbourg, France (DOI : 10.26093/cds/vizier). The original description of the VizieR service was published in 2000, A&AS 143, 23.

## References

- Alvarez-Candal, A., Pinilla-Alonso, N., Ortiz, J. L., et al. 2016, A&A, 586, A155  
 Assafin, M., Camargo, J. I. B., Vieira Martins, R., et al. 2012, A&A, 541, A142  
 Assafin, M., Vieira Martins, R., Camargo, J. I. B., et al. 2011, in *Gaia follow-up network for the solar system objects : Gaia FUN-SSO workshop proceedings*, 85–88  
 Barucci, M. A., Alvarez-Candal, A., Merlin, F., et al. 2011, Icarus, 214, 297  
 Barucci, M. A., Belskaya, I. N., Fulchignoni, M., & Birlan, M. 2005, AJ, 130, 1291  
 Barucci, M. A. & Merlin, F. 2020, Surface composition of Trans-Neptunian objects, ed. D. Prialnik, M. A. Barucci, & L. Young, 109–126  
 Benedetti-Rossi, G., Santos-Sanz, P., Ortiz, J. L., et al. 2019, AJ, 158, 159  
 Benedetti-Rossi, G., Sicardy, B., Buie, M. W., et al. 2016, AJ, 152, 156  
 Bierson, C. J. & Nimmo, F. 2019, Icarus, 326, 10  
 Braga-Ribas, F., Sicardy, B., Ortiz, J. L., et al. 2013, ApJ, 773, 26  
 Braga-Ribas, F., Sicardy, B., Ortiz, J. L., et al. 2014, Nature, 508, 72  
 Buie, M. W. & Keller, J. M. 2016, AJ, 151, 73  
 Camargo, J. I. B., Vieira-Martins, R., Assafin, M., et al. 2014, A&A, 561, A37  
 Chamberlain, M. A., Sykes, M. V., & Esquerdo, G. A. 2007, Icarus, 188, 451  
 Chandrasekhar, S. 1987, Ellipsoidal figures of equilibrium  
 Desmars, J., Camargo, J. I. B., Braga-Ribas, F., et al. 2015, A&A, 584, A96  
 Dias-Oliveira, A., Sicardy, B., Ortiz, J. L., et al. 2017, AJ, 154, 22

- Fernández, J. 2020a, Introduction: The Trans-Neptunian zone: past, present and future, ed. D. Prialnik, M. A. Barucci, & L. Young, 1–22
- Fernández, J. 2020b, Introduction: The Trans-Neptunian zone: past, present and future, ed. D. Prialnik, M. A. Barucci, & L. Young, 1–22
- Fornasier, S., Barucci, M. A., de Bergh, C., et al. 2009, *A&A*, 508, 457
- Fulchignoni, M., Belskaya, I., Barucci, M. A., de Sanctis, M. C., & Doressoundiram, A. 2008, *Transneptunian Object Taxonomy*, ed. M. A. Barucci, H. Boehnhardt, D. P. Cruikshank, A. Morbidelli, & R. Dotson, 181
- Gaia Collaboration, Brown, A. G. A., Vallenari, A., et al. 2018, *A&A*, 616, A1
- Gaia Collaboration, Brown, A. G. A., Vallenari, A., et al. 2016, *A&A*, 595, A2
- Gomes-Júnior, A. R., Giacchini, B. L., Braga-Ribas, F., et al. 2015, *MNRAS*, 451, 2295
- Grundy, W. M., Porter, S. B., Benecchi, S. D., et al. 2015, *Icarus*, 257, 130
- Hromakina, T. A., Belskaya, I. N., Krugly, Y. N., et al. 2019, *A&A*, 625, A46
- Johnston, W. R. 2018, *NASA Planetary Data System*
- Larsen, J. A., Roe, E. S., Albert, C. E., et al. 2007, *AJ*, 133, 1247
- Lomb, N. R. 1976, *Ap&SS*, 39, 447
- Müller, T., Lellouch, E., & Fornasier, S. 2020, *Trans-Neptunian objects and Centaurs at thermal wavelengths*, ed. D. Prialnik, M. A. Barucci, & L. Young, 153–181
- Noll, K., Grundy, W. M., Nesvorný, D., & Thirouin, A. 2020, *Trans-Neptunian binaries (2018)*, ed. D. Prialnik, M. A. Barucci, & L. Young, 201–224
- Ochsenbein, F., Bauer, P., & Marcout, J. 2000, *A&AS*, 143, 23
- Ortiz, J. L., Santos-Sanz, P., Sicardy, B., et al. 2017, *Nature*, 550, 219
- Ortiz, J. L., Sicardy, B., Camargo, J. I. B., Santos-Sanz, P., & Braga-Ribas, F. 2020, *Stellar occultation by TNOs: from predictions to observations*, ed. D. Prialnik, M. A. Barucci, & L. Young, 413–437
- Perna, D., Barucci, M. A., Fornasier, S., et al. 2010, *A&A*, 510, A53
- Plummer, H. C. 1919, *MNRAS*, 80, 26
- Press, W. H., Teukolsky, S. A., Vetterling, W. T., & Flannery, B. P. 1992, *Numerical recipes in FORTRAN. The art of scientific computing*
- Russell, C. T., Raymond, C. A., Ammannito, E., et al. 2016, *Science*, 353, 1008
- Sicardy, B., Ortiz, J. L., Assafin, M., et al. 2011, *Nature*, 478, 493
- Tancredi, G. & Favre, S. 2008, *Icarus*, 195, 851
- Thirouin, A., Noll, K. S., Ortiz, J. L., & Morales, N. 2014, *A&A*, 569, A3
- Thirouin, A., Ortiz, J. L., Duffard, R., et al. 2010, *A&A*, 522, A93
- Vachier, F., Berthier, J., Desmars, J., et al. 2019, *Central Bureau Electronic Telegrams*, 4703
- van Belle, G. T. 1999, *PASP*, 111, 1515
- Vilenius, E., Kiss, C., Müller, T., et al. 2014, *A&A*, 564, A35
- Zacharias, N., Monet, D. G., Levine, S. E., et al. 2004, in *American Astronomical Society Meeting Abstracts*, Vol. 205, American Astronomical Society Meeting Abstracts, 48.15

## Appendix A: Astrometry

Astrometric observations of Varda were performed by our group using several telescopes between 2013 and 2018. The observations used the ESO 2.2 m Max Planck telescope at La Silla (IAU code 809), the 1.6 m telescope at Laboratório Nacional de Astronomia, Pico dos Dias Observatory (IAU code 874) as well as the 1.5 m telescope at Sierra Nevada Observatory (IAU code J86).

The astrometric positions following these observations are given as ASCII supplementary material to the A&A paper. In this table, we indicate the date, the measured position (RA and DEC), observation site (IAU code), as well as the astrometric catalogue that was used as reference for the reduction.

## Appendix B: Explaining the observed gradual ingress and egress in the CAR data

In sub-section 4.3, we have modelled the observed gradual ingress and egress observed in the CAR station. The best-fitting model was obtained by introducing a non-instantaneous instrumental response. The latter is obtained by an (RC) electronic filter response ( $e^{-t/\tau}$ , where  $\tau$  is the capacitor's time constant) convolved with a rectangular function response that accounts for the finite integration time.

We attempt here to identify the physical/instrumental origin of this observed time delay. We first present an analysis of additional images taken a few minutes after the occultation, and conclude by giving a reason which can lead to the observed phenomenon.

Analysis of the after event video segment (~03:43 UT, about 5 minutes after the occultation) has shown a gradual dimming occurring clearly with the faint sources, while the brighter sources were not affected. Thanks to abrupt corrections on the pointing, as the FOV was drifting due to an imprecise telescope tracking, this could be identified. Fig. B.1 shows a sequence of 8 exposures taken between 03:43:54 and 03:44:02 UT (i.e., after occultation segment). Figure B.2 shows a smooth gradual disappearance of the phantom target star. We have successfully fit this gradual disappearance using the same instrumental response as in sub-section 4.3. The gradual ingress and egress during the occultation as well as the gradual disappearance of the phantom stars favour the hypothesis of an instrumental effect.

The recording Watec 910HX is an analog video camera widely used in the network of occultation observers worldwide. This low light video camera with integrating functions has an optional noise reduction filter named 3DNR (adjustable between 0 and 100%). This filter is activated at 50% level by default, and is automatically activated each time the camera settings are reset. The exact operation of this proprietary filter is unknown, but some tests and documentation have shown that it is a kind of running average filter, smoothing all the changes that occur at low light levels. For occultation work, this filter is turned off by the observers and this setting is normally kept in memory for the next uses.

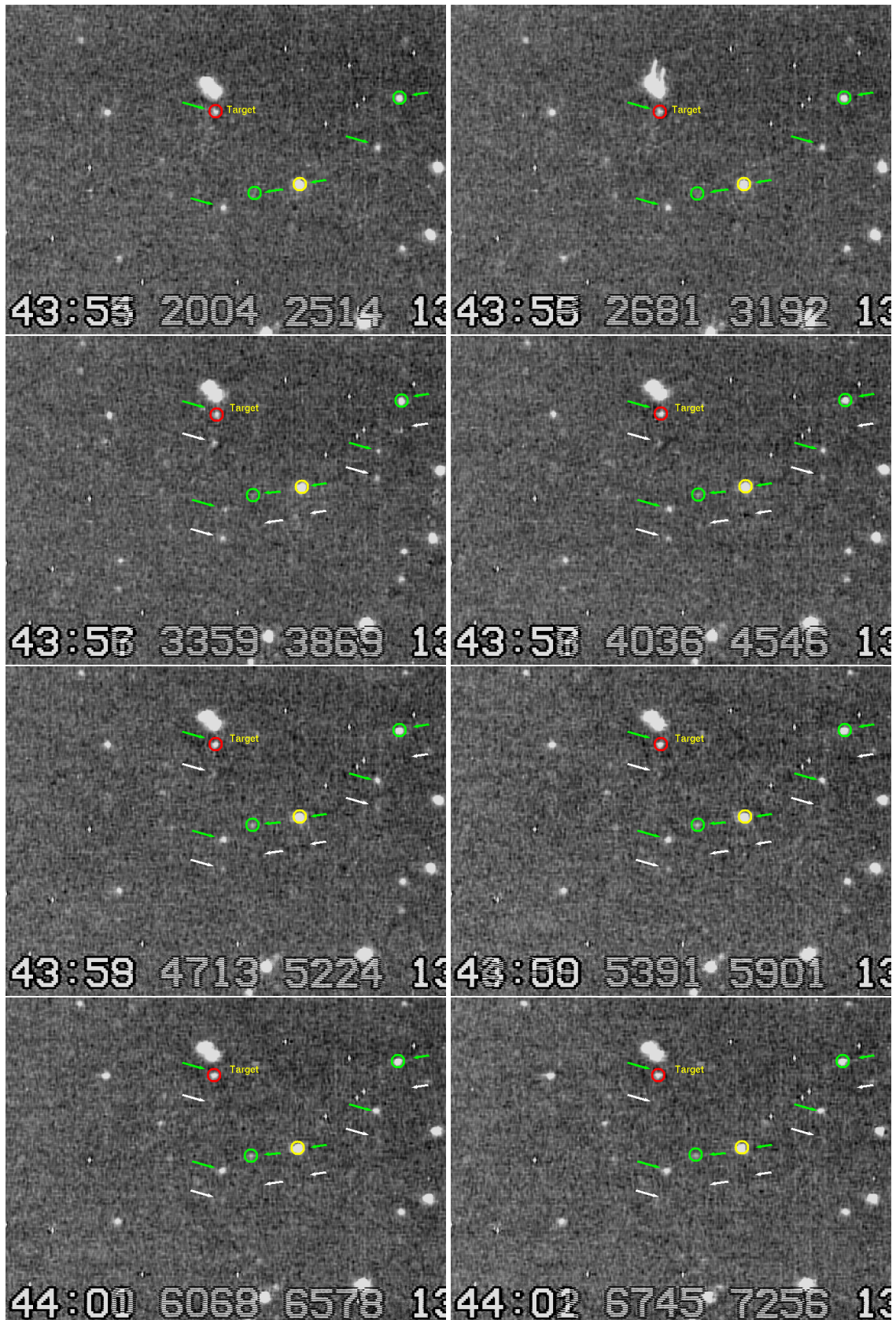
This gradual ingress/egress behaviour was recently observed during other stellar occultation events recorded by different observers using Watec 910HX cameras. In the light of this new data, we have performed several tests trying to explain this behaviour. Figure B.3 illustrates the results of tests that successfully reproduce the desired behaviour, namely the gradual dimming (over a few exposures) of the phantoms of the faint sources only.

To conclude, we have two reasons to think that the observed instrumental effects are caused by the 3DNR filter although the observer has no recollection nor knowledge of having it activated:

1. Cases of gradual occultation curves are regularly identified by IOTA coordinators to be the result of an unwanted activation of this filter. It appeared in particular that it is rather easy for the observer to reset the camera settings instead of exiting the camera menu, with the consequence of unintentionally reactivating the 3DNR filter.
2. Additional tests performed with a 910HX and a 3DNR filter at 50% level were able to reproduce the exact behaviour described in Fig. B.1. The same tests using a 3DNR filter set to off showed no anomaly.



Fig. B.1: This figure shows a sequence of 8 sub-frame images taken a few minutes after the event (between 03:43:54 and 03:44:02 UT). On each frame, the target star is circled in red while the guide and calibration stars are circled in yellow and green, respectively. Due to the tracking correction (because of imprecise telescope tracking), the stars move abruptly on the CCD during the exposure at 03:44:55 (on the sub-frame, we only see the minutes and the seconds). The green arrows point towards the real stars' positions. On the 03:43:57 exposure for example, we see "phantoms" of the dimmest stars (remnants from the previous exposures), which are shown by the white arrows. These phantoms are seen for at least five images, up to the 03:44:01 exposure.





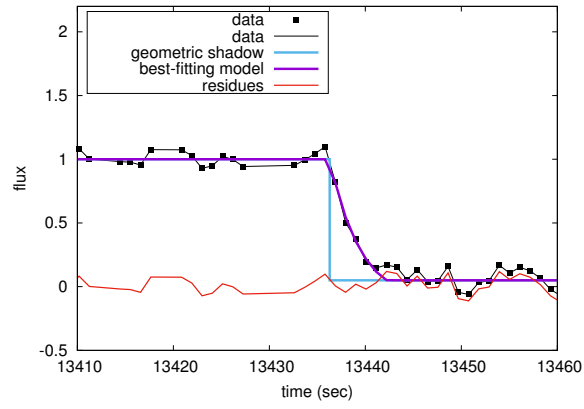


Fig. B.2: Gradual disappearance of the target's phantom modelled assuming an (RC) electronic filter response with a time constant  $\tau = 3.21$  s.

Fig. B.3: This figure shows 8 successive integrations of 1.28 s with a Watec 910HX and 3DNR set to ON at 50% level, during an abrupt correction of the star field centring. The green arrows point towards several faint reference stars. The white arrows point towards ghost images of these faint stars at their first position, fading gradually with time. Bright stars are not impacted by the filter.

